Hydrogen-anion formation near a (2×1)-reconstructed Si(100) surface: Substrate-electronic-structure and trajectory dependence

Boyan Obreshkov and Uwe Thumm

James R. Macdonald Laboratory, Department of Physics, Kansas State University, Manhattan, Kansas 66506-2604

We calculated the yield of outgoing hydrogen negative ions after the reflection of 1-keV neutral hydrogen atoms from a (2 × 1)-reconstructed Si(100) surface. We find that the charge-transfer dynamics at the reconstructed surface is dependent on both the surface-electronic structure and orientation of the projectile trajectory relative to the crystal azimuthal directions. Our results are in good quantitative agreement with the measured H⁻ fractions of Maazouz and Esaulov [Surf. Sci. **398**, 49 (1998)] for scattering trajectories that are aligned perpendicularly to rows of silicon dimers.

PACS number(s): 79.20.Rf

I. INTRODUCTION

Ion-surface scattering experiments [1] show that the formation of H⁻ near silicon and free-electron metal surfaces such as aluminum [2] is about equally likely and strongly dependent on the collision velocity of the incident projectile. For free-electron surfaces the details of the substrate-atomic structure are of little importance and may justify the modeling of charge transfer in the jellium approximation, which accounts for the surface-electronic structure solely in terms of the motion of a single active electron in the electric field of the uniformly smeared out positive charge of the substrate's ionic cores [3–5]. The final charge state of the projectiles after reflection from the surface is determined by electron capture into the affinity level (AL) of the hydrogen anion and electron loss to vacant substrate levels from the AL. Since electron affinities of negative ions are small compared to the work function of metals and typical semiconductors, the undistorted projectile AL is usually energetically in resonance with vacant levels above the Fermi level of the substrate, such that, in the absence of strong level shifts, the neutralization probability of a weakly interacting anion would be determined exclusively by electron loss. However, even at relatively large projectile-surface distances, i.e., for weak particle-surface interactions, exceptions to this unidirectional electron transfer occur if weakly bound image and surface states supported by the band structure of the substrate become degenerate with the weakly distorted projectile AL [6,7]. As the incident projectile moves closer to the surface, the projectile AL and weakly bound substrate levels experience more significant level shifts [3,8,9]. In this regime of strong coupling to the substrate, electronic levels of the adsorbate-substrate system may cross, adiabatically avoid crossing [9,10], and become subject to Pauli blocking as the occupied AL shifts into resonance with occupied substrate levels [6]. Furthermore, if the incident projectile speed is comparable to or larger than the Fermi velocity of the substrate, the modeling of electron-capture and -loss processes needs to account for kinematic level shifts [11,12]. For fast incident atoms, the inclusion of kinematic level shifts was found to be prerequisite for the quantitative agreement between calculated and measured negative-ion fractions on Al surfaces [2,5].

Even though measured negative-ion fractions on Si surfaces have the same magnitude as on Al surfaces, the jellium model is a poor approximation to the electronic structure of Si surfaces since the Si density of states is structured by narrow surface-state bands [13,14]. Indeed, in order to interpret their experimental results in Ref. [1], Maazouz *et al.* suggest that electron capture near Si surfaces is a dynamic, velocity-dependent, quasiresonant process that involves interactions of the projectile AL with a narrow band of surface states. A subsequent theoretical model for the formation of H⁻ on (2 × 1)-Si(100) and (7 × 7)-Si(111) reconstructed surfaces [15] reproduces the general trends of the measured hydrogen anion yield based on an appropriate parametrization of the Newns-Anderson model [16–19]. This theoretical investigation [15] found a strong dependence of the final projectile charge states on the scattering trajectories considered and reproduced the experimental data after averaging over trajectories.

A detailed study of the charge transfer between positive neon ions interacting with a CdS surface revealed a strong sensitivity of the ion-neutralization rates on the lateral corrugation of the target electronic density and on the chemical composition (i.e., on the Cd versus S termination) of the target [20,21]. Positive ions were less efficiently neutralized on the sulfur-terminated substrate and electron capture was found to be enhanced along closed-packed rows of Cd atoms on the Cd-terminated CdS surface. The dependence of the neutralization probability of Ne⁺ on the elemental composition of the substrate was confirmed theoretically within a rate-equation approach using static, laterally modulated electron-tunneling rates [21].

The theoretical investigation of the ionization (neutralization) of lithium atoms (ions) on reconstructed Si(100) surfaces [22] predicts a structural dependence of the static charge-transfer rates. Reconstruction was found to strongly influence the characteristics of the Li(2s) resonance state due to the lateral change of the target electron density. Charge transfer at the silicon substrate was found to depend on the electronic structure and morphology of the silicon substrate since ionization (neutralization) of Li (Li⁺) is enhanced near symmetric Si dimers, while charge transfer was predicted as unlikely in the buckled-dimer model for surface reconstruction. Similar structure-dependent and lateral-modulation effects were observed in the ionization of Li atoms on Al clusters [23]. Lateral changes of the AL width of H⁻ on free-electron vicinal surfaces were reported to cause

an enhancement of the anion-neutralization rates at surface steps [24]. These examples show that lateral modulation of the projectile-surface interaction entails site-specific and trajectory-dependent effects in the charge-transfer dynamics that influence the final charge state of a projectile after reflection on the surface.

In this work we follow up on these surface-structure and trajectory-dependent effects during charge transfer and discuss numerical results for the formation of H^- on (2×1)-reconstructed Si(100) surfaces. The paper is organized as follows. In Sec. II we review the Newns-Anderson model for one-electron charge transfer in ion-surface collisions. In Sec. III A we discuss the most relevant features of the static-electronic structure of the reconstructed Si(100) surface. In Sec. III B we present numerical results in the fixed-ion approximation (FIA), i.e., by analyzing charge transfer for a projectile at a fixed distance in front of the surface. In Sec. III C we consider hydrogen atoms with an incident kinetic energy of 1 keV and study the time evolution of their charge states during scattering along selected trajectories directed parallel or perpendicular to a row of Si dimers. Unless indicated otherwise, we use atomic units throughout this work ($e = \hbar = m_e = 1$).

II. THEORY

We describe the motion of the projectile classically, in terms of specific scattering trajectories $\mathbf{R}(t)$, and model the electronic dynamics during the projectile-surface interaction within the Newns-Anderson model [16–19] based on the Hamiltonian,

$$
\begin{aligned}
&H(\mathbf{R}(t)) \\
&= \varepsilon_a(\mathbf{R}(t)) \sum_\sigma c_{a\sigma}^\dagger c_{a\sigma} + \sum_{n,\sigma} \int_{\text{SBZ}} \frac{d^2\mathbf{k}_{||}}{(2\pi)^2} \varepsilon_n(\mathbf{k}_{||}) c_{n,\mathbf{k}_{||}\sigma}^\dagger c_{n,\mathbf{k}_{||}\sigma} \\
&\quad + \sum_{n,\sigma} \int_{\text{SBZ}} \frac{d^2\mathbf{k}_{||}}{(2\pi)^2} [V_{a,n\mathbf{k}_{||}}(\mathbf{R}(t)) c_{a\sigma}^\dagger c_{n,\mathbf{k}_{||}\sigma} + \text{H.c.}],
\end{aligned}
\tag{1}
$$

which owes its time dependence solely to the projectile motion $\mathbf{R}(t)$. The label n distinguishes electronic valence and conduction bands of the substrate, $\mathbf{k}_{||}$ is the parallel Bloch quasimomentum that changes over the first surface Brillouin zone (SBZ), and σ labels the component of the electronic spin along the surface normal. The anticommuting fermion operators $c_{a\sigma}$ and $c_{n,\mathbf{k}_{||}\sigma}$ annihilate electrons in the H^- affinity and substrate electronic states with energies ε_a and $\varepsilon_n(\mathbf{k}_{||})$, respectively, and $V_{a,n\mathbf{k}_{||}}$ denotes the spin-independent matrix elements for electron transfer between the substrate and the projectile. Direct transitions $V_{n'\mathbf{k}_{||}',n\mathbf{k}_{||}}$ among band-structure states are neglected, which is equivalent to orthogonalizing the AL wave function to the substrate orbitals as shown in Sec. II B.

The charge-transfer dynamics is given by Heisenberg's equations of motion

$$
i \frac{d}{dt} c_q(t) = [c_q, H(t)] = \sum_{q'} H_{qq'}(t) c_{q'}(t)
\tag{2}
$$

for $q \in \{a\sigma, \{n\mathbf{k}_{||}\sigma\}\}$. The expansion of the time-dependent operators $c_q(t)$ over unperturbed modes $c_q^0 = c_q(t_0)$,

$$
c_q(t) = \sum_{q'} S_{qq'}(t) c_{q'}^0,
\tag{3}
$$

leads to a system of coupled equations of motion

$$
i \frac{d}{dt} S_{qq'}(t) = \sum_{q''} H_{qq''}(t) S_{q''q'}(t)
\tag{4}
$$

for the transition amplitudes $S_{qq'}(t)$. These are subject to the initial conditions $S_{k'k}(t_0) = \delta_{k'k}$ for $\varepsilon_k \leqslant \varepsilon_F$, $S_{ak}(t_0) = 0$, $S_{ka}(t_0) = 0$, and $S_{aa}(t_0) = 1$, where ε_F is the Fermi level of the substrate and t_0 is a time long before the collision. The occupation numbers of the one-electron states at times $t > t_0$ are expressed in terms of the amplitudes as

$$
n_q(t) = \langle \Phi(t_0) | c_q^\dagger(t) c_q(t) | \Phi(t_0) \rangle = \sum_{q'} n_{q'}^0 |S_{qq'}(t)|^2,
\tag{5}
$$

where

$$
|\Phi(t_0)\rangle = \left(\prod_{\varepsilon_k \leqslant \varepsilon_F} c_k^\dagger(t_0) \right) c_a^\dagger(t_0) |\text{vac}\rangle
\tag{6}
$$

is the initial state of the electronic system and $|\text{vac}\rangle = |0,0,\ldots,0,\ldots\rangle$ is the vacuum state of noninteracting particles. The Pauli exclusion principle implies that electrons occupy different quantum states with occupation numbers $0 \leqslant n_q \leqslant 1$. In particular, the occupation of the anion state

$$
n_a(t) = n_a^0 |S_{aa}(t)|^2 + \sum_k n_k^0 |S_{ak}(t)|^2
\tag{7}
$$

is determined by the survival of the active electron in the initial anion state (first term) and electron capture from substrate bands (second term). Similarly, the substrate-level occupations

$$
n_k(t) = n_a^0 |S_{ka}(t)|^2 + \sum_{k'} n_{k'}^0 |S_{k'k}(t)|^2
\tag{8}
$$

have contributions due to electron loss from the projectile to the substrate (first term) and indirect continuum-continuum transitions between substrate levels $k \in \{n\mathbf{k}_{||}\sigma\}$ (second term).

The equations of motion [Eq. (4)] can be recast into a form that displays the coupling between the affinity and substrate levels,

$$
i \frac{d}{dt} S_{k'k}(t) = \varepsilon_{k'} S_{k'k}(t) + V_{k'a}(t) S_{ak}(t),
\tag{9}
$$

$$
i \frac{d}{dt} S_{k'a}(t) = \varepsilon_{k'} S_{k'a}(t) + V_{k'a}(t) S_{aa}(t),
\tag{10}
$$

$$
i \frac{d}{dt} S_{ak}(t) = \varepsilon_a(t) S_{ak}(t) + \sum_{k'} V_{ak'}(t) S_{k'k}(t),
\tag{11}
$$

$$
i \frac{d}{dt} S_{aa}(t) = \varepsilon_a(t) S_{aa}(t) + \sum_k V_{ak}(t) S_{ka}(t).
\tag{12}
$$

The elimination of the final substrate channels by time integration results in

$$
S_{k'k} = e^{-i\varepsilon_{k'}(t-t_0)} \delta_{k'k} + \int_{t_0}^t dt' e^{-i\varepsilon_{k'}(t-t')} V_{k'a}(t') S_{ak}(t')
\tag{13}
$$

and

$$S_{k'a}(t) = \int_{t_0}^{t} dt' e^{-i\varepsilon_k(t-t')} V_{k'a}(t') S_{aa}(t'). \qquad (14)$$

Substitution of Eqs. (13) and (14) into Eqs. (11) and (12), respectively, leads to the set of uncoupled integrodifferential Volterra equations

$$i\frac{d\tilde{S}_{aq}(t)}{dt} = \int_{t_0}^{t} dt' \tilde{\Sigma}_{aa}(t,t') \tilde{S}_{aq}(t') + \tilde{V}_{aq}(t'), \qquad (15)$$

with the definitions

$$\tilde{S}_{aq}(t) = \exp\left(i\int_{t_0}^{t} dt' \varepsilon_a(t')\right) S_{aq}(t), \qquad (16)$$

the retarded self-energy kernel for the AL

$$\tilde{\Sigma}_{aa}(t,t') = -i\sum_{k} \tilde{V}_{ak}(t)\tilde{V}_{ak}^{*}(t'), \qquad (17)$$

given in terms of the matrix elements for negative-ion formation

$$\tilde{V}_{aq}(t) = (1-\delta_{aq})\exp\left(i\int_{t_0}^{t} dt' \omega_{ak}(t')\right) V_{ak}(t), \qquad (18)$$

and the transition frequencies between adsorbate and substrate energy levels $\omega_{ak}(t) = \varepsilon_a(t) - \varepsilon_k$.

A. Fixed-ion approximation

In FIA the time scales for the electronic dynamics and the motion of the projectile are assumed to be so far apart that the electronic distribution has time to fully equilibrate for any fixed position **R** of the projectile along its scattering trajectory. In this limit the analysis of the electronic dynamics simplifies significantly since the couplings to the substrate become time independent.

Setting $t_0 = 0$ and using the Laplace transformation of the transition amplitudes in Eqs. (9)–(12),

$$G_{q'q}(z) = \int_{0}^{\infty} dt\, e^{-zt} S_{q'q}(t) \qquad (19)$$

leads, in FIA, to equations of motion for the amplitudes $G_{q'q}$,

$$(iz - \varepsilon_{k'})G_{k'k}(z) - V_{k'a}G_{ak}(z) = \delta_{k'k}, \qquad (20)$$

$$(iz - \varepsilon_k)G_{ka}(z) - V_{ka}G_{aa}(z) = 0, \qquad (21)$$

$$(iz - \varepsilon_a)G_{aa}(z) - \sum_{k} V_{ka}G_{ak}(z) = 1, \qquad (22)$$

$$(iz - \varepsilon_a)G_{ak}(z) - \sum_{k'} V_{ak'}G_{k'k}(z) = 0, \qquad (23)$$

with solutions

$$\begin{aligned} G_{k'k}(z) &= G_{k'}^{0}(z)[\delta_{k'k} + V_{k'a}G_{ak}(z)], \\ G_{k'a}(z) &= G_{k'}^{0}(z)V_{k'a}G_{aa}(z), \\ G_{ak}(z) &= G_{aa}(z)V_{ak}G_{k}^{0}(z), \\ G_{aa}(z) &= [iz - \varepsilon_a - \Sigma_a(z)]^{-1}. \end{aligned} \qquad (24)$$

These solutions are given in terms of the retarded AL self-energy function

$$\Sigma_a(z) = \sum_{k} \frac{|V_{ak}|^2}{iz - \varepsilon_k}, \quad \text{Re}[z] > 0, \qquad (25)$$

the unperturbed propagators of target electrons $G_k^0(z) = (iz - \varepsilon_k)^{-1}$, and the perturbed propagator $G_{aa}(z)$ of the projectile electron. The amplitudes $S_{qq'}(t)$ are obtained by an inverse Laplace transformation,

$$S_{q'q}(t) = \frac{1}{2\pi i}\int_{C} dz\, e^{zt} G_{q'q}(z), \qquad (26)$$

where C is a straight-line path in the complex z plane parallel to the imaginary z axis with $\text{Re}[z] = \eta$, η is an infinitesimal positive constant.

The complex poles $z_n = -i\varepsilon_n - \Gamma_n/2$ of the Green's function, analytically continued onto the second Riemann sheet of complex energy, correspond to the quasistationary or resonance states of the adsorbate system. The resonance that correlates asymptotically to the undistorted AL is called the AL resonance. By taking the limit $\eta \to 0$, the self-energy splits into its real and imaginary parts according to $\Sigma_a(-i\varepsilon + 0) = \Lambda_a(\varepsilon) - i\Delta_a(\varepsilon)$, where

$$\Delta_a(\varepsilon) = \pi\sum_{k} |V_{ak}|^2 \delta(\varepsilon - \varepsilon_k) \qquad (27)$$

is the chemisorption width function and

$$\Lambda_a(\varepsilon) = -\frac{1}{\pi}\text{P}\int d\varepsilon' \frac{\Delta_a(\varepsilon')}{\varepsilon' - \varepsilon} \qquad (28)$$

the chemisorption shift function (P designates Cauchy principal value integral). The projected density of states (PDOS) of the interacting system,

$$\rho_a(\varepsilon) = -\frac{1}{\pi}\text{Im}G_{aa} = \frac{1}{\pi}\frac{\Delta_a(\varepsilon)}{[\varepsilon - \varepsilon_a - \Lambda_a(\varepsilon)]^2 + \Delta_a^2(\varepsilon)}, \qquad (29)$$

is the density of admixture of the anionic state into the continuum of target states of energies ε. For a substrate with a large bandwidth and weakly energy-dependent PDOS, the shift function Λ_a is usually negligible. In this case the PDOS distribution is an isolated Lorentzian with a half width at half maximum $\Gamma_a/2 = \Delta_a$, which corresponds to the static AL decay width due to electron tunneling into the substrate. In the opposite limit, when the adsorbate is interacting with a narrow band of substrate states, $\Lambda_a(\varepsilon)$ may acquire a considerable magnitude and energy dependence and the PDOS distribution may split into a pair of peaks corresponding to the bonding and antibonding adsorbate resonance levels. We determine the resonance energies ε_n and decay widths Γ_n in the FIA by χ^2 fitting the PDOS distribution to a superposition of Breit-Wigner resonance profiles

$$\rho_a(\varepsilon) \approx \sum_{n} Z_n \frac{\Gamma_n/2\pi}{(\varepsilon - \varepsilon_n)^2 + (\Gamma_n/2)^2}, \qquad (30)$$

where Z_n are position-dependent amplitude factors.

B. Implementation of the Newns-Anderson model for moving ions

1. Orbitals and matrix elements

In order to specify all orbital energies and coupling matrix elements in the Newns-Anderson Hamiltonian in Eq. (1), we first compute the ground-state electron density $n_{\rm TF}$ and screened single-particle pseudopotential of the unperturbed Si substrate

$$v_s(\mathbf{r}) = v_{\rm core}(\mathbf{r}) + \int d^3\mathbf{r}' \frac{n_{\rm TF}(\mathbf{r}')}{|\mathbf{r} - \mathbf{r}'|} + \frac{\delta E_{\rm xc}^{\rm LDA}}{\delta n(\mathbf{r})}\bigg|_{n=n_{\rm TF}} \quad (31)$$

in Thomas-Fermi–von Weizsäcker approximation [24–26]. The first term in v_s is the local unscreened pseudopotential of the Si ionic cores and $E_{\rm xc}^{\rm LDA}$ is the exchange-correlation energy of the electron gas in local-density approximation. For our numerical calculations we employ an empirical core potential [27] $v_{\rm core}$, represent the exchange energy in Dirac approximation [28], and use the Wigner parametrization for the correlation energy [29]. Given the orbital-free Thomas-Fermi electron density $n_{\rm TF}$, we numerically solve the single-particle Schrödinger equation

$$\left(-\tfrac{1}{2}\nabla_\mathbf{r}^2 + v_s(\mathbf{r})\right)\varphi_k(\mathbf{r}) = \varepsilon_k\varphi_k(\mathbf{r}) \quad (32)$$

to obtain the substrate electronic wave functions φ_k with energies ε_k [30]. The wave functions

$$\varphi_k(\mathbf{r}) = e^{i\mathbf{k}_\| \cdot \mathbf{r}_\|} u_{n,\mathbf{k}_\|}(\mathbf{r}) \quad (33)$$

are Bloch wave functions of definite parallel quasimomentum $\mathbf{k}_\|$, where the functions $u_{n,\mathbf{k}_\|}$ exhibit the periodicity of the crystal in the surface plane,

$$u_{n,\mathbf{k}_\|}(\mathbf{r}) = \sum_{\mathbf{G}_\|} c_{n,\mathbf{G}_\|+\mathbf{k}_\|}(z)e^{i\mathbf{G}_\|\cdot\mathbf{r}_\|}, \quad (34)$$

$\{\mathbf{G}_\|\}$ are the surface reciprocal lattice wave vectors, and z is the electronic coordinate normal to the surface.

Introducing the hydrogenic core potential $v_p(\mathbf{r})$, the full Hamiltonian of the active electron can be cast into the form

$$h_\mathbf{r}(t) = -\tfrac{1}{2}\nabla_\mathbf{r}^2 + v_s(\mathbf{r}) + v_p(\mathbf{r} - \mathbf{R}(t)). \quad (35)$$

We approximate the projectile potential by a regularized zero-range Fermi potential [31,32],

$$v_p(\mathbf{r}) = \frac{2\pi}{\alpha}\delta^{(3)}(\mathbf{r})\frac{\partial}{\partial r}r, \quad (36)$$

with $\alpha = \sqrt{-2\varepsilon_a}$. This contact potential holds a single bound state with energy $\varepsilon_a^0 = -0.75$ eV equal to the hydrogen electron affinity and corresponding wave function

$$\varphi_{a_0}(\mathbf{r}) = \sqrt{\frac{\alpha}{2\pi}}\frac{e^{-\alpha r}}{r}. \quad (37)$$

The orbital φ_a is not orthogonal to the substrate orbitals φ_k, but can be orthogonalized by the redefinition

$$|a\rangle = |a_0\rangle - \sum_k |k\rangle\langle k|a_0\rangle, \quad (38)$$

leading to the transition matrix elements

$$V_{ak} = \langle a_0|v_p|k\rangle - \sum_{k'}\langle a_0|k'\rangle\langle k'|v_p|k\rangle. \quad (39)$$

In our case, since direct transitions among band-structure states $\langle k'|v_p|k\rangle = 0$ are neglected, the transition matrix elements simplify to

$$V_{ak} = \langle a_0|v_p|k\rangle. \quad (40)$$

We approximate the projectile level shift

$$\varepsilon_a(\mathbf{R}(t)) = \langle a|h_\mathbf{r}(t)|a\rangle \approx \varepsilon_a^0 - \frac{1}{4Z(t)}\frac{\epsilon(0) - 1}{\epsilon(0) + 1} \quad (41)$$

by including only the electrostatic attraction of the active electron to its induced image charge on the substrate. We use $\epsilon(0) = 11.9$ for the static bulk dielectric constant of Si [33] and neglect the lateral variation of the electric self-image potential by retaining its dependence on the distance $Z(t)$ of the projectile nucleus from the first atomic layer of the surface.

2. Frame transformation

The matrix elements V_{ak} are evaluated in a substrate-fixed Galilean frame of reference. Since the wave function of the negative-ion AL is defined in the rest frame of the projectile, we Galilei transform the projectile-centered wave function to the surface-fixed frame by multiplying it with an electron-translation factor (ETF) [34–36]

$$\tilde{\varphi}_{a_0}(\mathbf{r},t) = e^{i(\mathbf{v}\cdot\mathbf{r}-\mathbf{v}^2 t/2)}\varphi_{a_0}(\mathbf{r} - \mathbf{R}(t))e^{-i\varepsilon_a^0 t}, \quad (42)$$

where $\mathbf{v} = \mathbf{v}(t = +\infty)$ is the asymptotic projectile velocity after reflection at the surface. The ETF incorporates the correct outgoing boundary condition in the negative-ion formation channel. Our choice of the asymptotic outgoing projectile velocity in the ETF is an approximation for the incident part of the projectile trajectory that becomes accurate in the limit of grazing incidence, $v_\| \gg v_n$, where $v_\|$ and v_n are the components of the projectile velocity in the surface plane and in the direction perpendicular to the surface, respectively. This choice is supported by the loss of memory of the projectile charge state along the incident trajectory we find in our numerical results (see Sec. III C below).

Subject to this transformation, the active electron acquires a momentum $\mathbf{v}$ and the AL shifts kinematically according to $\varepsilon_a^0 \to \varepsilon_a^0 + \mathbf{v}^2/2$. The transition matrix element

$$V_{ak}(t) = \langle\tilde{a}_0(t)|v_a|k\rangle = \sqrt{2\pi\alpha}e^{-i\mathbf{v}\cdot\mathbf{R}(t)}\varphi_{n,\mathbf{k}_\|}(\mathbf{R}(t)) \quad (43)$$

factorizes into a product of a velocity-dependent phase factor and an electronic-structure-dependent factor.

3. Projectile trajectory

The center-of-mass motion of the projectile is treated classically, based on Newton's equation of motion,

$$M\frac{d^2\mathbf{R}}{dt^2} = -\nabla_\mathbf{R}U(\mathbf{R}), \quad (44)$$

where $M = 1837m_e$ is the projectile mass and $U(\mathbf{R})$ is the scattering potential, which we model as a superposition of repulsive Thomas-Fermi-Molière interatomic potentials [37,38],

$$U(\mathbf{R}) = Z_t Z_p \sum_{\mathbf{R}_t}\sum_{k=1}^3 a_k \frac{e^{-b_k|\mathbf{R}-\mathbf{R}_t|/a_F}}{|\mathbf{R}-\mathbf{R}_t|}, \quad (45)$$

and $\mathbf{R}_t$ are the position vectors of the substrate-atomic cores. For the given nuclear charges of substrate and projectile cores, $Z_t = 14$ and $Z_p = 1$, the Firsov screening length is $a_F = 0.8853(Z_t^{1/2} + Z_p^{1/2})^{-2/3} = 0.3137$ and the remaining parameters are $\{a_k\} = \{0.35, 0.55, 0.1\}$ and $\{b_k\} = \{0.3, 1.2, 6.0\}$.

4. Geometry and numerical representation of the (2 × 1)-reconstructed Si(100) surface

We represent the effects of surface reconstruction within the symmetric dimer model [39]. According to this model, Si atoms in the first atomic layer of the unreconstructed substrate move pairwise toward each other and form dimers. The symmetric Si dimers are oriented, their bonds forming rows in the surface plane. We model the substrate crystal in a periodically replicated slab geometry. The slab represents a finite piece of the substrate with sufficient thickness to reproduce the bulk valence properties of the Si crystal. The unit supercell shown in Fig. 1(a) consists of 13 layers of Si cores plus a vacuum region equivalent to 6 layers of Si in thickness. The height of the slab is $25a_0/4$, where $a_0 = 10.263$ is the bulk lattice constant for Si.

The irreducible quarter of the SBZ, together with the four high-symmetry points, is shown in Fig. 1(b). We sample one-half of the entire SBZ by including $N_{\mathbf{k}_{||}} = 40$ wave vectors in the irreducible part of the SBZ and calculate the wave functions of 75 bands up to the vacuum energy level. We thus include $40 \times 75 = 3000$ discrete, closely spaced energy levels in this calculation. We employ a plane-wave basis set of size $(N_x, N_y, N_z) = (2^4, 2^3, 2^6)$ for the representation of the orbital-free density $n_{\mathrm{TF}}(\mathbf{r})$ and integrate numerically over the

surface area A_{SBZ} of the SBZ according to

$$\frac{1}{A_{\mathrm{SBZ}}} \int_{\mathrm{SBZ}} \frac{d^2\mathbf{k}_{||}}{(2\pi)^2} \rightarrow \frac{1}{N_{\mathbf{k}_{||}}} \sum_{\mathbf{k}_{||}}. \qquad (46)$$

Figures 1(c) and 1(d) show the scattering geometry and surface projections of two trajectories that are aligned either parallel or perpendicular to rows of dimer bonds on the reconstructed surface.

III. NUMERICAL RESULTS AND DISCUSSION

A. Static-electronic structure of the substrate

The unreconstructed Si surface exhibits two broken bonds per surface atom from which two surface-state bands arise: the dangling-bond band and the dimerlike bridge band [30]. These two bands are only partially occupied in the ground state of the surface. In the (2 × 1)-reconstructed surface, atoms in the surface layer have moved pairwise to form rows of aligned symmetric dimers. Thus half of the broken bonds of the clean unreconstructed surface rebond after reconstruction. In Fig. 2(a) we show the Thomas-Fermi charge density $n_{\mathrm{TF}}(\mathbf{r})$ of the (2 × 1)-reconstructed surface in Eq. (31). The density is enhanced at the dimer bonds, which exhibit slightly larger amplitudes than the bulk Si-Si bonds.

Figure 2(b) shows the screened single-particle pseudopotential $v_s(\mathbf{r})$ derived from the Thomas-Fermi density according to Eq. (31). The band structure supported by the screened potential is displayed in Fig. 3. The distribution of energy levels exhibits a band gap near the Fermi level. Two bands of surface states (indicated by dashed lines in Fig. 3) are found inside the gap with energies near the Fermi energy. They change in a similar way as functions of the quasimomentum $\mathbf{k}_{||}$. The lower-energy surface state is partially occupied with a bandwidth of 1.15 eV. Our calculation based on the Thomas-Fermi approach predicts a splitting between the two bands of about 1 eV measured from the band bottoms, while angle-integrated photoemission measurements [13] indicate a splitting of only 0.5 eV. This discrepancy may be due to the dimer-bond length we used as input for our calculation. However, the dispersion relation we obtain for these states is in good agreement with other theoretical results for the electronic
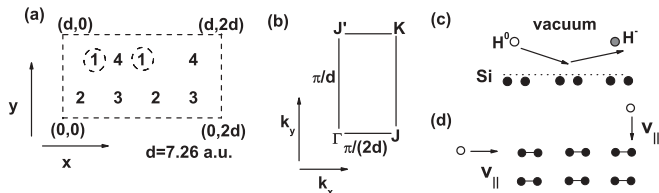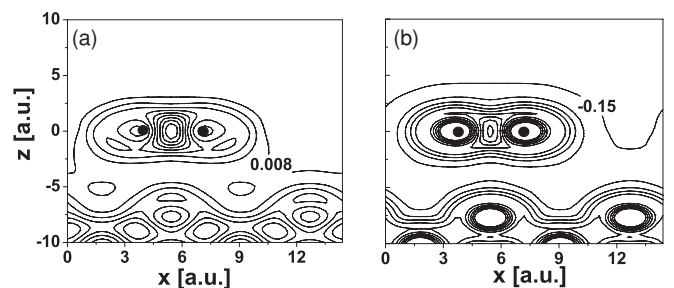

FIG. 1. (a) Orientation of the first four atomic planes of the (2 × 1)-reconstructed Si(100) surface, viewed from the vacuum side in the direction normal to the surface. The unit cell is denoted by straight dashed lines. The numbers label the layer where Si atomic cores are located: 1 is the first surface layer, 2 is the second layer, etc. Surface layers are separated by the distance $a_0/4$, where $a_0 = 10.263$ is the bulk lattice constant of the silicon crystal. Except for the first surface layer, the nearest neighbors in a given plane are separated by $d = a_0/\sqrt{2}$. The (2 × 1) reconstruction affects the arrangement of atoms in layer 1, i.e., silicon atoms move pairwise in the X direction and form dimers of bond length $d/2$. The numbers enclosed in circles represent impact locations of select scattering trajectories discussed in this work. (b) Irreducible part of the surface Brillouin zone with the four high-symmetry points corresponding to the planar unit cell. The Cartesian coordinates of these points are $\Gamma = (0.000, 0.000)$, $J = (0.216, 0.000)$, $K = (0.216, 0.433)$, and $J' = (0.000, 0.433)$. (c) Scattering geometry: Incident neutral hydrogen atoms emerge as hydrogen anions after reflection form the surface. $\mathbf{v}_{||}$ designates the surface projection of the collision velocity. Our numerical examples are restricted to projectiles directed (c) parallel or (d) perpendicular to Si-dimer rows.

FIG. 2. Contour map of (a) the ground-state charge density of the (2 × 1)-reconstructed Si(100) surface and (b) the screened single-particle pseudopotential $v_s(\mathbf{r})$. The graphs show the vacuum region on top and extended six layers into the bulk. The contour line spacing is (a) 0.008 a.u. and (b) 0.15 a.u. Only negative values of v_s relative to the vacuum energy level are shown in (b). The positions of the Si-atomic cores in the first surface layer are indicated by dots.
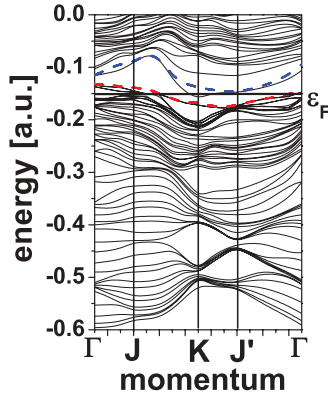
FIG. 3. (Color online) Surface band structure of the (2×1)-reconstructed Si surface in the symmetric dimer model. The band structure is shown along a close contour connecting (by straight lines) the four high-symmetry end points in the irreducible part of the surface Brillouin zone. In the gap region near the Fermi level ($\varepsilon_F = -0.152$ a.u.), the surface-state bands of π bonding and antibonding π^* orbitals are given by the upper (blue) and lower (red) dashed lines, respectively.

structure of reconstructed Si surfaces. The calculated splitting is between 1.5 and 2 eV according to Refs. [40,41] and about 1 eV according to Ref. [42].

The charge densities of the two surface states are shown in Fig. 4 at three points on a straight-line path between the two high-symmetry end points J and K. The densities exhibit molecular π-orbital character due to hybridization of atomic sp_z dangling bonds of the unreconstructed surface. In the zeroth-order approximation, linear combinations of the sp_z states on the left and right Si atoms are degenerate and have opposite reflection parities. During the reconstruction,

Si atoms move pairwise to each other, as their dangling-bond wave functions mix, giving rise to the even π bonding and odd π^* antibonding dimer-dangling-bond bands shown in Fig. 4.

The amplitude of the bonding π states progressively weakens near the surface as the quasimomentum $k_y \rightarrow 0$ [Figs. 4(a)–4(c)], while the electron in this state is transferred into the bulk [Fig. 4(c)]. Near the J point, π orbitals are promoted above the Fermi level by approximately 1 eV, which is nearly equal to the width of the π band. In contrast, we find that the π^* band does not significantly change its antibonding character as a function of the quasimomentum $\mathbf{k}_{||}$ along the same path in the SBZ [Figs. 4(d)–4(f)].

B. Fixed-ion approximation

The PDOS $\rho_a(\varepsilon)$ is shown in Figs. 5(a)–5(d) for fixed projectile-surface distances Z relative to the position of the first atomic layer. The lateral position of the adsorbate atom is fixed on top of the Si-dimer atom as shown in the inset. At large distances $Z = 10$ [Fig. 5(a)], where the interaction with the surface-electronic structure is weak, the PDOS contains a single sharp Lorentzian peak corresponding to the AL resonance. The energy distribution of the AL resonance does not extend below the Fermi level. As the distance to the surface decreases to $Z = 4$ [Fig. 5(b)], a broad resonance structure develops in the PDOS. At $Z = 3$ [Fig. 5(c)] the PDOS splits into a pair of resonance peaks separated by a gap. The lower-energy affinity-level resonance, which emerges below the Fermi level, is energetically degenerate with bulk valence bands. In view of this opposite bonding character and to simplify the notation, we designate the energetically lower resonance state by $|\overline{\text{AL}}\rangle$. At small chemisorption distances the two resonance states are relatively short lived, with level widths of 0.5 eV. In close proximity to the first surface layer,
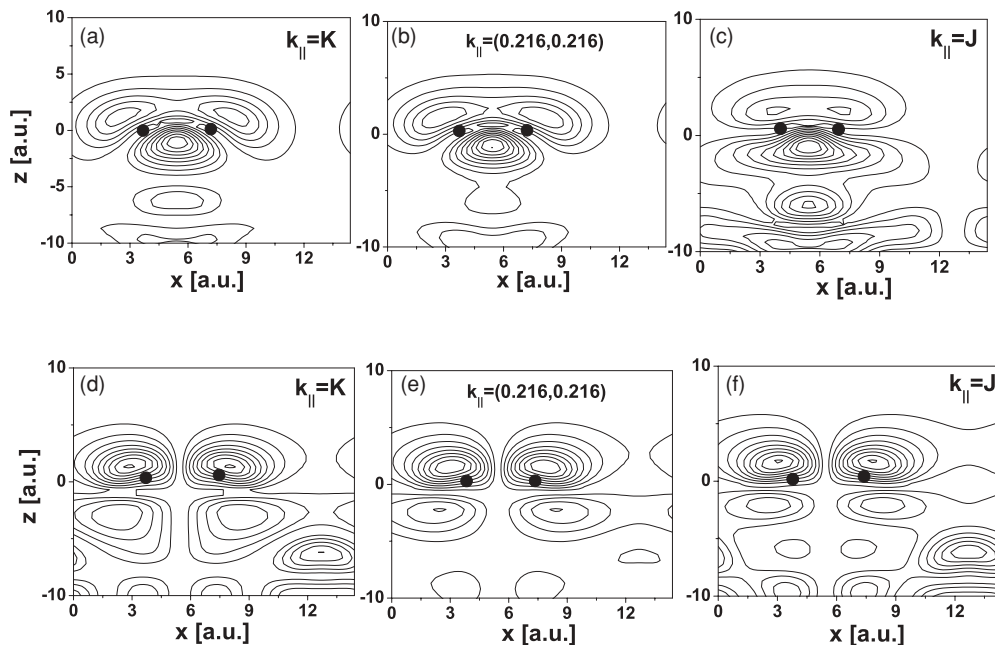

FIG. 4. Charge densities of (a)–(c) π bonding and (d)–(f) π^* antibonding surface states on the (2×1)-reconstructed Si(100) surface. The first 4.5 layers are shown. The parallel Bloch momentum $\mathbf{k}_{||}$ changes along a straight-line path connecting the high-symmetry end points K and J in the surface Brillouin zone. The positions of the Si cores forming the surface dimer are represented by the dots.
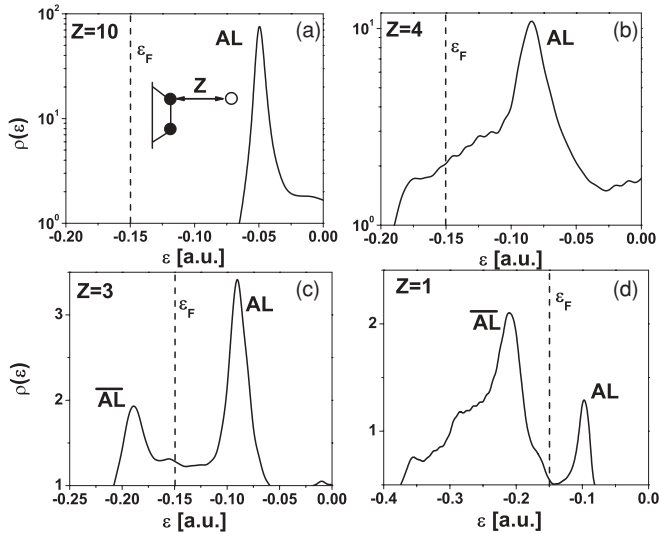
FIG. 5. Density of states projected onto the affinity-level orbital of H^- for fixed normal H-surface distances Z. The lateral position of the projectile is on top of a Si-dimer atom. AL designates the antibonding affinity-level resonance and $\overline{AL}$ denotes the lower-energy bonding affinity-level resonance. (a) $Z = 10$, (b) $Z = 4$, (c) $Z = 3$, and (d) $Z = 1$ a.u. The vertical dashed lines in (a)–(d) indicate the position of the Fermi level at $\varepsilon_F = -0.152$ a.u.

FIG. 6. (Color online) Results in the fixed-ion approximation, i.e., for fixed but variable distances Z normal to the surface. The lateral position of the hydrogen atom is fixed on top of a silicon-dimer atom, as shown in the inset in (c). (a) Contour plot of the chemisorption width $\Delta_a(\varepsilon, Z)$ of the adsorbate system. (b) Density of states $\rho_a(\varepsilon, Z)$ projected onto the affinity-level orbital of H^-. The upper (red) and lower (blue) arrows point to the AL and $\overline{AL}$ resonance, respectively. (c) Energy levels of the hydrogen affinity-level resonances states near the (2×1)-reconstructed Si(100) surface. The higher-energy resonance is the antibonding AL resonance (closed-circle line) and the lower-energy resonance is the bonding $\overline{AL}$ resonance (closed-triangle line). The projectile (open circle) interacts with a Si dimer (closed circles). The solid line shows the image-potential shifted affinity level $\varepsilon_a(Z)$ of H^-. The dashed line indicates the position of the Fermi level of the Si surface. (d) Static level width of the hydrogen affinity-level resonance states near the (2×1)-reconstructed Si(100) surface. The same symbol notation is used as in (c): closed-circle line gives static level width of the antibonding AL resonance and the closed-triangle line gives the decay width of the bonding AL resonance.

at $Z = 1$ [Fig. 5(d)], the center of the higher-energy AL resonance distribution has saturated at approximately 2 eV above the Fermi level and its has become narrower. At the same time, spectral weight in the PDOS is seen to transfer to the lower-energy bonding $|\overline{AL}\rangle$ resonance, which overlaps the energetically broader bulk resonance structures.

Contour plots of the chemisorption width function $\Delta_a(\varepsilon, Z)$ and the PDOS $\rho_a(\varepsilon, Z)$ are shown in Figs. 6(a) and 6(b), respectively, for a fixed lateral position of the adsorbate atom on top of a Si-dimer atom. At large distances to the surface, the chemisorption width function in Fig. 6(a) is concentrated near the conduction bands. As Z decreases, the distribution peaks in the band-gap region, indicating strong hybridization with the surface-state bands. Similarly, the PDOS distribution has distinct contributions from conduction bands at large distances to the surface [Fig. 6(b)]. The center of the distribution moves toward lower energies as the distance Z decreases due to the attractive image-charge interactions. The width of the PDOS is narrow over this range of physisorption distances and dominated by the long-lived antibonding $|AL\rangle$ resonance. At smaller distances, the hybridization with the surface-state bands causes a redistribution in the PDOS, which splits near $Z = 4$. The center of the higher-energy part of the distribution changes slowly with the decrease of distance Z and saturates at the upper edge of the band gap since the hydrogen-anion affinity cannot penetrate the forbidden gap region (see also Fig. 3). At the same time, spectral weight shifts across the Fermi level into the lower-energy part of the distribution. At very small distances ($Z < 2$) the PDOS distribution peaks near and below the lower edge of the occupied surface-state band due to contributions of the lower-energy bonding $|\overline{AL}\rangle$ resonance state.
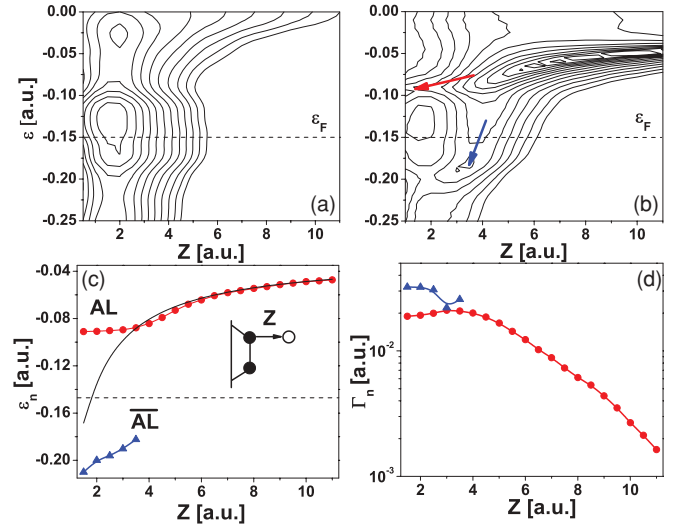
The static energy positions and widths of the pair of AL resonance states are shown in Figs. 6(c) and 6(d). At large distances to the surface, the AL level shifts toward the Fermi level due to image-charge interactions and is long lived, with a lifetime of $\tau_{AL} = \Gamma_{AL}^{-1} \geqslant 100$. The neutralization rate of the negative ion is comparable to its neutralization rate near free-electron surfaces, which, in the jellium approximation, is given by $\Gamma_{AL}^{(jellium)}(Z = 6) \approx 0.2$ eV [7,10]. Near $Z \approx 5$ the energy of the AL starts to deviate from the pure image shift and eventually saturates for even smaller distances at approximately 2 eV above the Fermi level. At the same time, hybridization interactions to surface-state bands cause the appearance of the lower-energy bonding affinity-level resonance $|\overline{AL}\rangle$, which is relatively short lived with a lifetime $\tau_{\overline{AL}} \geqslant 50$ a.u. At small chemisorption distances $Z \approx 3$, neutralization rates of negative ions at free-electron surfaces are larger by a factor of 5 such that AL resonance states are relatively long lived near the reconstructed Si surface. The occupied bonding affinity-level resonance state $|\overline{AL}\rangle$ shares the anion character and becomes energetically accessible for charge transfer at small distances to the surface. With regard to the dynamic situation discussed in Sec. III C, we note that the
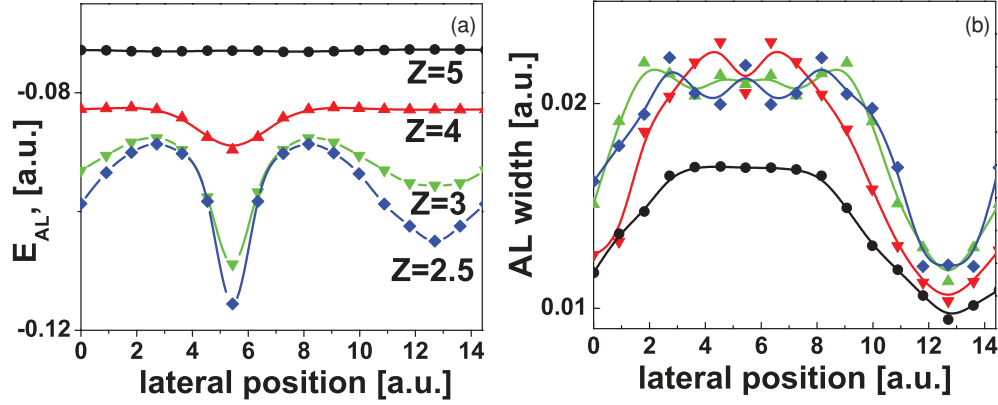
FIG. 7. (Color online) Change of the (a) energy and (b) width of the antibonding hydrogen affinity-level resonance near the (2×1)-reconstructed Si(100) surface as a function of the lateral position X for different fixed H-surface distances Z, measured relative to the first surface layer: $Z = 5$ (circles), $Z = 4$ (upper triangles), $Z = 3$ (lower triangles), and $Z = 2$ a.u. (diamonds).

repulsive interaction between the $|AL\rangle$ and $|\overline{AL}\rangle$ resonance states suggests two possible pathways for the negative-ion formation that both contribute to the final population of the affinity level: the active electron may either (i) remain in the energetically higher $|AL\rangle$ resonance by adiabatically avoiding crossing with the lower-energy $|\overline{AL}\rangle$ resonance or (ii) populate the AL from promoted valence-band states.

Surface reconstruction affects the characteristics of the resonance states, which become sensitive to the nonuniformity and lateral change of the target electron density. In Fig. 7(a) the lateral corrugation of the energy level of the AL resonance as a function of the reconstruction coordinate X is shown for fixed positions Z normal to the surface. The X axis is oriented along dimer rows and the X-Z plane intersects dimer atoms in the top layer [labeled 1 in Fig. 1(a)]. At close distances to the surface $Z \leqslant 3$ a.u., the lateral level shift is significant, ~ 1 eV. The energy level attains a local minimum at the middle of a dimer bond, while interactions with individual dimer atoms are repulsive, and the AL exhibits maxima at the positions of Si atoms in the first surface layer. The lateral change of the AL width is shown in Fig. 7(b). The effect of the corrugation of the AL width is negligible; however, near Si dimers the width develops tiny but rapid lateral oscillations. The AL width follows, on average, the characteristics of the (2×1) surface morphology. The wave function of resonance states can be evaluated using the expansion over basis states (see Ref. [43])

$$\psi_n(\mathbf{r}; \mathbf{R}) = \sqrt{Z_n} \left(\varphi_a(\mathbf{r}; \mathbf{R}) + \sum_k \frac{V_{ak}(\mathbf{R})}{E_n(\mathbf{R}) - \varepsilon_k} \varphi_k(\mathbf{r}) \right),$$
(47)

where $E_n(\mathbf{R}) = \varepsilon_n(\mathbf{R}) - i\Gamma_n(\mathbf{R})/2$ are the complex resonance energies, Z_n are normalization factors

$$Z_n(\mathbf{R}) = \left(1 + \sum_k |V_{ak}(\mathbf{R})|^2 / [E_n(\mathbf{R}) - \varepsilon_k]^2 \right)^{-1}, \quad (48)$$

and

$$|\varphi_a\rangle = \frac{1}{\sqrt{1 - \sum_k |\langle k|a_0\rangle|^2}} \left(|a_0\rangle - \sum_k |k\rangle\langle k|a_0\rangle \right) \quad (49)$$

is the Gram-Schmidt orthogonalized state of the hydrogen-negative-ion affinity.

The charge density of the AL resonance states are shown in Figs. 8(a) and 8(b) for the chemisorption distance $Z = 3.5$ and for a projectile located on top of a Si-dimer atom. Charge transfer in the direction normal to the surface is blocked and the active electron tunnels into the bulk through the middle of the Si dimer at a small angle relative to the inward surface normal. Near the surface, wave functions of the surface-state bands spread laterally. The electronic density of the bonding AL resonance protrudes parallel to the surface and extends over three times the size of a single Si dimer. Induced weak interdimer correlations are noticeable. In contrast, the more compact electronic distribution of the antibonding AL resonance results from hybridization of the π^* and conduction-band states. The lateral corrugation and orientation dependence of the projectile-surface interactions in the FIA suggests that charge transfer at the reconstructed surface will exhibit the directional character of the dimer formation and depend on the alignment of the surface-projected trajectory relative to the azimuthal axis of the crystal.

C. Charge-transfer dynamics

Allowing for the motion of the projectile in the calculation of the charge-transfer dynamics, we numerically solve the equations of motion [Eq. (15)]. Using the Nystrom method [44], we discretize Eq. (15) on an equidistant time mesh, with N points and spacings $h = T/N$, that extends over a time interval T. Both N and T are chosen sufficiently large to guarantee numerical convergence. We evaluate the time integrals in Eqs. (15) and (18) by trapezoidal quadrature and approximate the time derivative by two-point finite differences. The initial conditions correspond to neutral hydrogen atoms approaching the substrate at a collision energy of 1 keV. The occupation number of the AL of H^- prior to the collision is $n_a(t_0) = 0$. After the collision it can be written as an overlap of two energy distributions [45]

$$n_a = \int d\varepsilon \, n^0(\varepsilon) S(\varepsilon), \quad (50)$$
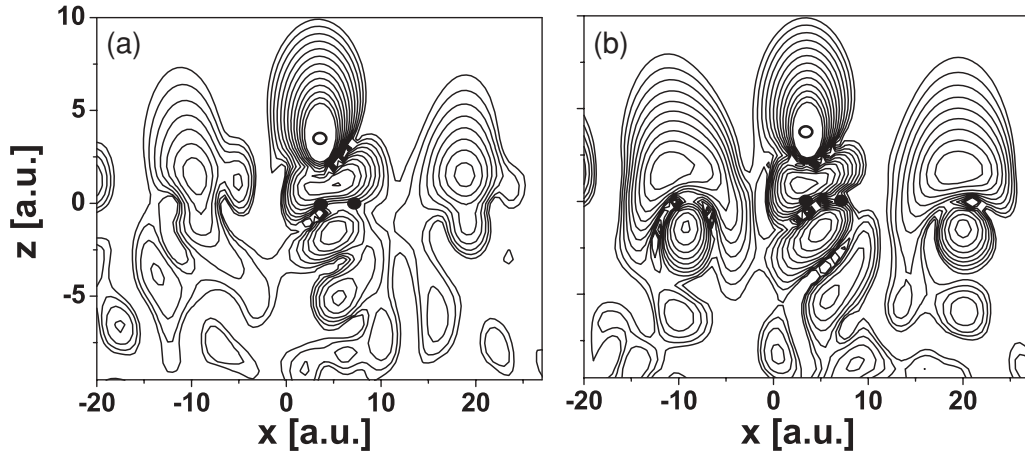
FIG. 8. Contour map of the charge density for the (a) $|AL\rangle$ and (b) $|\overline{AL}\rangle$ affinity-level resonance states of H$^-$ near the (2×1)-reconstructed Si(100) surface. The position of the projectile at the distance $Z = 3.5$ a.u. on top of Si-dimer atoms (solid circles) is indicated by the open circle.

where

$$S(\varepsilon) = \sum_k |S_{ak}|^2 \delta(\varepsilon - \varepsilon_k) \qquad (51)$$

is the tunneling density of states (TDOS) projected onto the affinity-level orbital and $n^0(\varepsilon) = \theta(\varepsilon_F - \varepsilon)$ is the Fermi-Dirac distribution function at zero surface temperature.

1. Negative-ion formation and memory effects

Figure 9(a) shows the modulus of the self-energy kernel $|\Sigma(t,t')|$ for two grazingly incident trajectories with incidence angle $\Theta_{inc} = 5°$. The trajectories are directed either parallel ($\Phi_{inc} = 0°$) or perpendicular ($\Phi_{inc} = 90°$) to rows of Si dimers, where Φ_{inc} is the angle of alignment of the incident trajectories relative to the [100] crystal direction. $\tilde{\Sigma}(t,t')$ is the amplitude for the active electron to tunnel into and out of the continuum
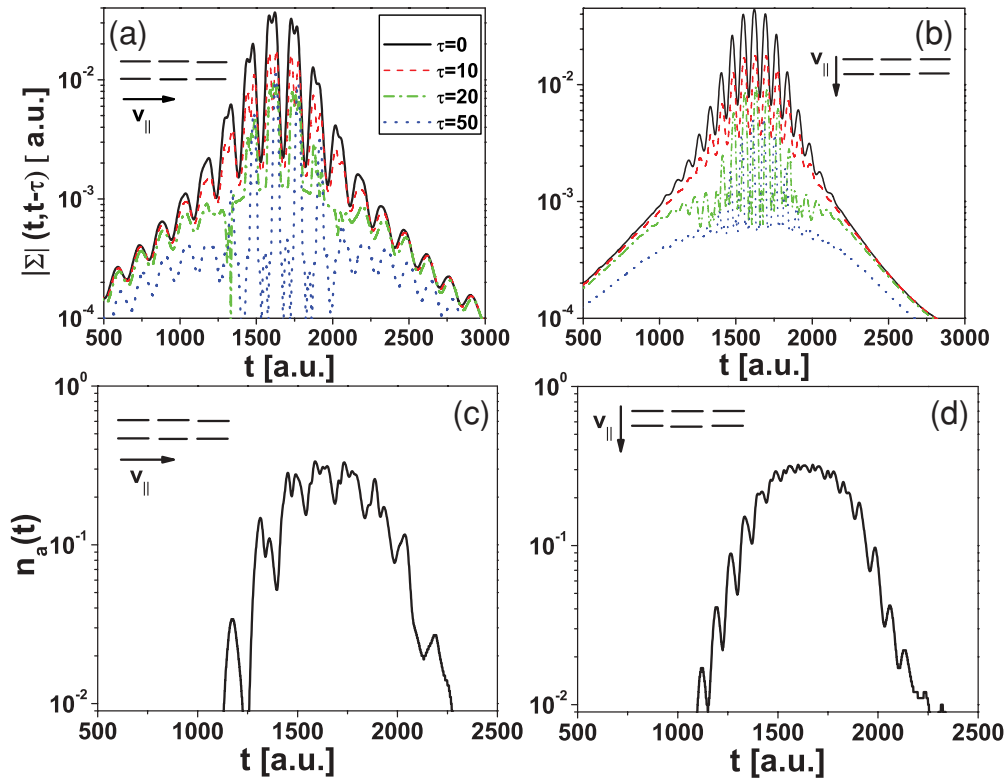

FIG. 9. (Color online) (a) Amplitude of the electronic self-energy kernel near the (2×1)-reconstructed Si(100) surface as a function of time t. The parameter τ characterizes the range over which the system holds a memory of its previous charge state. The kernel is evaluated for grazingly incident projectiles with $\Theta_{inc} = 5°$ directed parallel to rows of Si dimers. (b) Same as (a) for grazingly incident projectiles directed perpendicularly to rows of dimer bonds. (c) Occupation of the affinity level of the hydrogen anion $n_a(t)$ as a function of time for the trajectory in (a). (d) $n_a(t)$ for the trajectory in (b).

of target states during the time interval $\tau = t - t'$. If τ is shorter than the characteristic time for the parallel motion $T_{||} = d/2v_{||} \approx 20$ (given by the dimer-bond length $d/2$ and the velocity component in the surface plane $v_{||}$), the self-energy amplitude develops a temporal modulation with the period of the reconstructed surface lattice of ionic cores. This is best understood in the limit $\tau \to 0$, where the self-energy function can be expressed by the integrated static fixed-ion chemisorption width [Eq. (27)],

$$\tilde{\Sigma}(t,t) = \frac{1}{\pi i} \int d\varepsilon \, \Delta_a(\varepsilon, \mathbf{R}(t)), \tag{52}$$

as an expression of the irreversible electron loss from the AL into valence and conduction bands of the substrate.

For finite time intervals $\tau > 0$, the system develops a memory of its previous charge state. The amplitude of the self-energy kernel is seen to decrease exponentially over time on a scale of $\tau < 20$, which approximately corresponds to the inverse width of the Si-surface band gap [see also Fig. 6(a)]. For time intervals $\tau > 20$, the superimposed oscillatory structure is due to interference of electron tunneling into and out of different substrate states. However, since the strength of these interactions is suppressed by more than a factor of 2, as compared to the strength of short-time correlations, we expect the electronic system to adjust quasiadiabatically to the motion of the projectile at this collision energy. Similar effects are found for incident projectiles that move perpendicularly to dimer rows [Fig. 9(b)]. The major difference is caused by surface reconstruction, which changes the distribution of scattering centers experienced by the projectile.

The occupation number $n_a(t)$ of the projectile level as a function of time is shown in Figs. 9(c) and 9(d) for the two trajectories discussed in Figs. 9(a) and 9(b), respectively. Prior to reflection from the surface, electron capture from the valence bands accumulates charge on the negative ion. Very close to the surface, the projectile moves at a constant speed $v_{||}$ parallel to the surface, interacting with many Si atoms. The negative-ion fractions stabilize near $n_a \approx 30\%$ during large time interval of 500 a.u. and charge states oscillate over time following the lateral period of the (2×1) reconstruction. After reflection, electron loss to conduction-band states of the substrate prevails and negative-ion formation is unlikely [Figs. 9(c) and 9(d)], with the occupation number n_a being less than 1%. To investigate the dependence of charge transfer on the collision velocity $\mathbf{v}$, we further focus on the effect of electron-translation phase factors used in our computation.

2. Kinematic level shifts

In Figs. 10(a)–10(d) we show the negative-ion occupation numbers $n_a(t)$ for different scattering trajectories of common impact location aligned perpendicularly to a row of Si dimers ($\Phi_{inc} = 90°$) and for angles of incidence $\Theta_{inc} \in [5°, 90°]$ relative to the surface normal. For normal incidence $\Theta_{inc} = 90°$ [Fig. 10(a)], we find that the exclusion of the ETF affects the negative-ion yields on the incident part of the trajectory; however, final outgoing negative-ion yields are independent of the translation phase factor. By decreasing the angle of incidence to $\Theta_{inc} = 45°$ [Fig. 10(b)], we do not find qualitative changes in outgoing negative-ion yields. The negative-ion
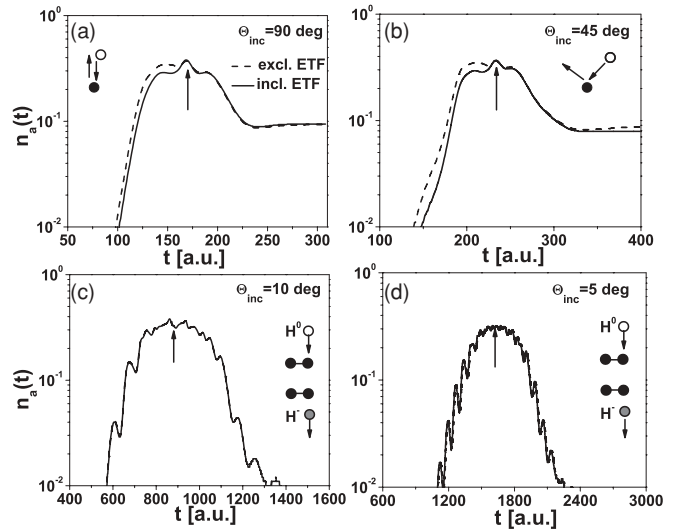

FIG. 10. Occupation of the affinity level near the (2×1)-reconstructed Si(100) surface. The dashed (solid) lines are theoretical results with (without) the electron translation phase factor. The collision energy is 1 keV. The angles of incidence Θ_{inc} are (a) 90°, (b) 45°, (c) 10°, and (d) 5°. The time of closest approach on the trajectory of the projectile is indicated by the arrows.

yields are large for normal incidence ($n_a \approx 10\%$), indicating that target electrons are efficiently promoted into the AL of the projectile during the collision. As the projectiles become grazingly incident, with $\Theta_{inc} \leqslant 10°$ [Figs. 10(c) and 10(d)], the anion fractions stabilize with $n_a \leqslant 1\%$ and are not changed by the exclusion of the ETF.

Using Eq. (40), we can write the anion-formation matrix element for grazing incidence as

$$\tilde{V}_{ak}(t) \approx \sqrt{2\pi\alpha}\exp\left(i\int_0^t dt'\,\varepsilon_a(t')\right) u_{n,\mathbf{k}_{||}}(\mathbf{R}(t))e^{-i(\varepsilon_{n,\mathbf{k}_{||}} - \mathbf{k}_{||}\cdot\mathbf{v}_{||})t}, \tag{53}$$

clearly exposing a lateral Doppler shift of the substrate energy levels

$$\varepsilon_{n,\mathbf{k}_{||}} \to \varepsilon_{n,\mathbf{k}_{||}} - \mathbf{k}_{||} \cdot \mathbf{v}_{||}. \tag{54}$$

If the quasimomentum $\mathbf{k}_{||}$ is antiparallel to the projectile velocity, $\mathbf{k}_{||} \cdot \mathbf{v}_{||} < 0$, valence-band levels can shift upward above the Fermi level. Since the quasimomentum is defined up to a wave vector $\mathbf{G}_{||}$ of the surface reciprocal lattice, substrate levels can experience even more significant shifts $(\mathbf{k}_{||} + \mathbf{G}_{||}) \cdot \mathbf{v}_{||}$ and become resonant with the AL at intermediate and large distances to the surface, thereby enabling electron capture [11] [Fig. 10(c)].

3. Dependence on the surface dimer orientation

We now focus on the dependence of charge transfer on the orientation of the parallel velocity vector $\mathbf{v}_{||}$ relative to dimer axis of the crystal. For grazing or nearly grazingly incident projectiles ($\Theta_{inc} \leqslant 20°$), which are moving perpendicularly to Si-dimer bonds ($\Phi_{inc} = 90°$), the characteristic shift of the target levels near the J' point of the SBZ is $\delta\varepsilon_k = v_{||}k_{||}^{(J')} \approx 0.4 \times 0.2 = 0.08$ [for $\mathbf{G}_{||} = (0,0)$]. For projectiles moving parallel to a row of dimer bonds ($\Phi_{inc} = 0°$), the surface reconstruction reduces the typical level shift by a factor of

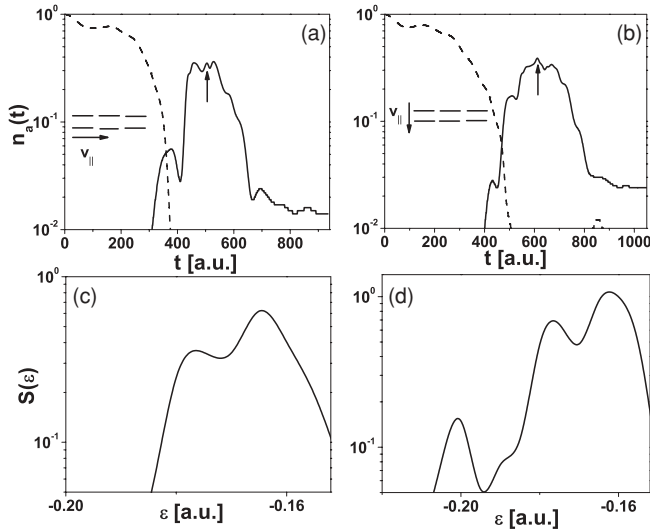FIG. 11. Occupation of the affinity level of H^- near the (2×1)-reconstructed Si(100) surface. Dashed lines in (a) and (b) give anion-survival probabilities $|S_{aa}|^2$. Solid lines are the probabilities for electron capture. The collision energy is 1 keV. The point of closest approach on the trajectory is indicated by the arrow. (a) Projectiles directed parallel to rows of Si dimers at an angle of incidence $\Theta_{inc} = 18°$. The exit angle is $\Theta_{exit} = 20°$. (b) Projectiles directed perpendicularly to dimer rows at an incidence angle $\Theta_{inc} = 14°$. The exit angle is $\Theta_{exit} = 30°$. (c) Tunneling density of states $S(\varepsilon)$ along the trajectory in (a) (see the text for further detail). (d) $S(\varepsilon)$ for the trajectory in (b).

$2, \delta\varepsilon_k = v_{||}k_{||}^{(J)} \approx 0.2 \times 0.2 = 0.04$. This structure-dependent effect is also seen in Figs. 11(a) and 11(b), where negative-ion occupation numbers are shown for two trajectories directed parallel and perpendicular to a dimer row, respectively. The projectiles have a dominant parallel velocity component $v_{||} \approx 0.19$. The angle of incidence is $\Theta_{inc} = 18°$ for the trajectory in Fig. 11(a) and $14°$ for the trajectory in Fig. 11(b). The exit angle to the surface is $\Theta_{exit} \approx 20°$ for the trajectory in Fig. 11(a) and $\Theta_{exit} \approx 30°$ for the second nonspecular trajectory in Fig. 11(b).

The ion-survival factors $|S_{aa}|^2$ in Figs. 11(a) and 11(b) show that the loss of memory of initial charge states occurs prior to reflection from the surface, while final negative-ion yields are determined by electron capture from the target. Prior to reflection from the surface, valence electrons undergo transitions into the AL of the negative ion, where electronic charge accumulates and oscillates over a time interval of more than 200 a.u. Near the point of closest approach to the surface, the occupation number of the projectile level reaches a maximum of $n_a = 40\%$ on both trajectories. After the reflection from the surface, electron loss to conduction-band states entails a reduction of the projectile charge over a time interval of approximately 100 a.u. The decay of anion fractions after the reflection is not purely exponential over time and shows transient oscillations. The negative-ion fractions saturate at larger physisorption distances to the surface ($Z > 5$). For projectiles that move perpendicularly to dimer rows, the final negative-ion fraction is $n_a \approx 3\%$ [Fig. 11(b)], while for surface-projected trajectories that are parallel to dimer rows it is $n_a = 1.5\%$ [Fig. 11(a)].
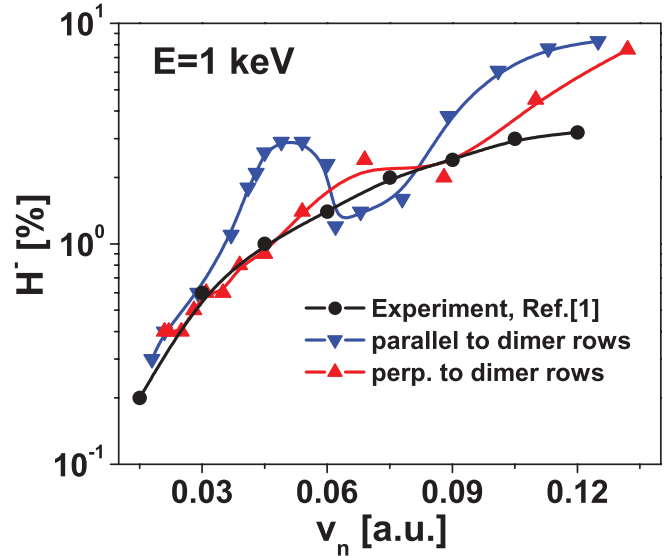

FIG. 12. (Color online) Negative-hydrogen-ion yields on the (2×1)-reconstructed Si(100) surface as a function of the exit velocity component normal to the surface v_n. The collision energy is 1 keV. Corresponding incidence angles are in the range $\Theta_{inc} \in [3°, 25°]$. Upward pointing triangles give final anion yields for projectiles moving perpendicularly to Si-dimer rows. Inverted triangles correspond to trajectories oriented parallel to dimer rows [cf. Fig. 1(d)]. Circles show the measured [1] negative-ion yields on Si surfaces.

In Figs. 11(c) and 11(d) we show the TDOS distribution $S(\varepsilon)$ [Eq. (51)] for these two scattering trajectories. As both figures demonstrate, the main contributions to the negative-ion formation involve transitions from the narrow surface-state band of π electrons, which undergo promotion across the band gap into the AL of H^- (cf. Fig. 5).

The final negative-ion yield as a function of the exit velocity v_n normal to the surface is shown in Fig. 12 for trajectories reflecting on the first atomic layer, parallel or perpendicular to rows of Si dimers [cf. Fig. 1(c)]. The angle of incidence Θ_{inc} is between $3°$ and $25°$ and the corresponding exit angles Θ_{exit} are between $3°$ and $45°$. The measured outgoing negative-ion fraction on Si surfaces in Ref. [1] is also shown for a collision energy of 1 keV. The negative-ion fractions are nonmonotonic functions of the exit velocity v_n and depend on the orientation of the surface-projected trajectory relative to the azimuthal axis of the crystal. For scattering parallel to the dimer row, outgoing fractions oscillate with the exit velocity v_n. For $v_n \gtrsim 0.1$, nonspecular reflection results in increased negative-ion fractions. For scattering trajectories perpendicular to dimer rows and reflecting quasispecularly from the surface with $v_n < 0.1$, we find that our calculated negative-ion fraction quantitatively reproduces the experimental v_n dependence in Ref. [1].

Despite the very good quantitative agreement of the experimental data with the prediction of the Newns-Anderson model for scattering along low Miller-index orientations of the crystal, we need to mention that the measurements of outgoing negative-ion fractions in Ref. [1] were performed for varying orientations of the crystal sample relative to the direction of the incident projectile beam. The projectiles were directed at incidence angles $\Theta_{in} \in [2°, 36°]$ and outgoing fractions

were sampled for exit angles $\Theta_{exit} \in [3°,40°]$, leading to measured negative-ion yields below 7%. We therefore assume that the experiment includes mainly trajectories that reflect (almost) specularly from the surface. We further note that for nonspecular reflections and large exit angles $\Theta_{exit} > 45°$, our calculated negative-ion fractions do not exceed 12% for any azimuthal orientation of the crystal, providing evidence for the validity of our model.

IV. CONCLUSION

We calculated the fraction of negative hydrogen ions after the reflection of 1-keV incident neutral hydrogen atoms from the (2×1)-reconstructed Si (100) surface. We find that charge-transfer rates depend sensitively on the projectile trajectory, surface morphology, and characteristics of the reconstruction. For grazingly incident projectiles directed perpendicular to silicon dimer rows, our calculated hydrogen-negative-ion fractions reproduce the measured fractions in Ref. [1] for outgoing projectiles with normal exit velocities $v_n \in [0.01, 0.1]$.

[1] M. Maazouz, L. Guillemot, V. A. Esaulov, and D. J. O'Connor, Surf. Sci. **398**, 49 (1998).

[2] M. Maazouz, A. G. Borisov, V. A. Esaulov, J. P. Gauyacq, L. Guillemot, S. Lacombe, and D. Teillet-Billy, Phys. Rev. B **55**, 13869 (1997).

[3] P. Nordlander and J. C. Tully, Phys. Rev. B **42**, 5564 (1990).

[4] P. Kürpick, U. Thumm, and U. Wille, Phys. Rev. A **56**, 543 (1997).

[5] A. G. Borisov, D. Teillet-Billy, and J. P. Gauyacq, Phys. Rev. Lett. **68**, 2842 (1992).

[6] H. Chakraborty, T. Niederhausen, and U. Thumm, Phys. Rev. A **70**, 052903 (2004).

[7] H. Chakraborty, T. Niederhausen, and U. Thumm, Phys. Rev. A **69**, 052901 (2004).

[8] J. Burgdörfer, E. Kupfer, and H. Gabriel, Phys. Rev. A **35**, 4963 (1987).

[9] P. Kürpick and U. Thumm, Phys. Rev. A **58**, 2174 (1998).

[10] A. G. Borisov, A. K. Kazansky, and J. P. Gauyacq, Phys. Rev. B **59**, 10935 (1999).

[11] U. Thumm and J. S. Briggs, Nucl. Instrum. Methods B **43**, 471 (1989).

[12] H. Winter, Phys. Rep. **367**, 387 (2002).

[13] F. J. Himpsel and D. E. Eastman, J. Vac. Sci. Technol. **16**, 1297 (1979).

[14] C. Kentsch, M. Kutschera, M. Weinelt, T. Fauster, and M. Rohlfing, Phys. Rev. B **65**, 035323 (2001).

[15] E. A. García, C. González, P. G. Bolcato, M. C. G. Passegi, and E. C. Goldberg, Surf. Sci. **600**, 2195 (2006).

[16] P. W. Anderson, Phys. Rev. **124**, 41 (1961).

[17] R. Brako and D. M. Newns, Rep. Prog. Phys. **52**, 655 (1989).

[18] J. Burgdörfer, in *Review of Fundamental Processes and Applications of Atoms and Ions*, edited by C. D. Lin (World Scientific, Singapore, 1993), p. 517.

[19] A. Nourtier, in *Electronic Processess at Solid Surfaces*, edited by E. Ilisca and K. Makoshi (World Scientific, Sinagpore, 1996), p. 85.

[20] L. Houssiau, J. W. Rabalais, J. Wolfgang, and P. Nordlander, Phys. Rev. Lett. **81**, 5153 (1998).

[21] L. Houssiau, J. W. Rabalais, J. Wolfgang, and P. Nordlander, J. Chem. Phys. **110**, 8139 (1999).

[22] K. Niedfeldt, P. Nordlander, and E. A. Carter, Surf. Sci. **601**, L29 (2007).

[23] M. Taylor and P. Nordlander, Phys. Rev. B **64**, 115422 (2001).

[24] B. Obreshkov and U. Thumm, Surf. Sci. **601**, 622 (2007).

[25] C. A. Utreras-Diaz, Phys. Rev. B **36**, 1785 (1987).

[26] E. Zaremba and H. C. Tso, Phys. Rev. B **49**, 8147 (1994).

[27] M. Schlüter, J. R. Chelikowsky, S. G. Louie, and M. L. Cohen, Phys. Rev. B **12**, 4200 (1975).

[28] B. Obreshkov and U. Thumm, Phys. Rev. A **74**, 012901 (2006).

[29] N. D. Lang and W. Kohn, Phys. Rev. B **1**, 4555 (1970).

[30] B. Obreshkov and U. Thumm, Phys. Rev. A **76**, 052902 (2007).

[31] K. Huang and C. N. Yang, Phys. Rev. **105**, 767 (1957).

[32] K. Wòdkiewicz, Phys. Rev. A **43**, 68 (1991).

[33] N. W. Ashcroft and N. D. Mermin, *Solid State Physics* (Thomson Learning, London, 1976).

[34] D. R. Bates and R. McCarroll, Proc. R. Soc. London Ser. A **245**, 175 (1958).

[35] W. Fritsch, in *Review of Fundamental Processes and Applications of Atoms and Ions* (Ref. [18]), p. 239.

[36] J. Merino, N. Lorente, M. Yu. Gusev, F. Flores, M. Maazouz, L. Guillemot, and V. A. Esaulov, Phys. Rev. B **57**, 1947 (1998).

[37] G. Moliére, Z. Naturforsch. **2**a, 133 (1947).

[38] J. J. Ducrée, F. Casali, and U. Thumm, Phys. Rev. A **57**, 338 (1998).

[39] H. E. Farnsworth, R. E. Schiller, T. H. George, and R. M. Burger, J. Appl. Phys. **26**, 252 (1955).

[40] J. A. Appelbaum, G. A. Baraff, and D. R. Hamann, Phys. Rev. B **14**, 588 (1975).

[41] J. A. Appelbaum, G. A. Baraff, and D. R. Hamann, Phys. Rev. B **15**, 2408 (1977).

[42] Z. Zhu, N. Shima, and M. Tsukada, Phys. Rev. B **40**, 11868 (1989).

[43] R. M. More and E. Gerjuoy, Phys. Rev. A **7**, 1288 (1973).

[44] W. H. Press, S. A. Tekuolsky, W. T. Vetterling, and B. P. Flannery, *Numerical Recipes in FORTRAN* (Cambridge University Press, Cambridge, 1993).

[45] A. Nourtier, J. Phys. France **50**, 311 (1989).